ACS APPLIED NANO MATERIALS

www.acsanm.org

Article

Pristine Nanostructured α-Ni(OH)$_2$ as a Nonenzymatic Electrochemical Strip Sensor for Trace Detection of Phenolic Compounds

Suman Mondal, Aritra Roy, Rene Pfeifer, Felipe Fantuzzi,* Amitava Choudhury,* and Kalisadhan Mukherjee*

Cite This: *ACS Appl. Nano Mater.* 2025, 8, 20463−20476

Read Online

ACCESS | Metrics & More | Article Recommendations | Supporting Information

ABSTRACT: Developing electrochemical sensors capable of detecting multiple analytes at distinct potentials is vital for applications in environmental, biomedical, and quality monitoring. Here, we explore nanostructured, nonenzymatic α-Ni(OH)$_2$ as a versatile sensing material for the selective detection of phenol, catechol, and *p*-nitrophenol using two platforms: a standard three-electrode system and a portable strip sensor. α-Ni(OH)$_2$ was synthesized via a wet-chemical method and coated onto glassy carbon and screen-printed carbon electrodes for the respective configurations. Electron microscopy confirmed semicrystalline nanoscale morphology (nanoparticulate films), and cyclic voltammetry revealed clear redox signatures for each analyte, enabling selective detection with distinct peak positions across both systems. The three-electrode setup reached limits of detection of 0.003 μM (phenol), 0.1 μM (catechol), and 1 μM (*p*-nitrophenol), whereas the portable sensor achieved 0.3, 1, and 2 μM, respectively. Amperometric measurements confirmed sensor performance at target potentials. Additionally, machine learning algorithms were applied to model signal behavior and support analyte classification. This combined approach demonstrates a robust strategy for sensitive, selective, and portable detection of multiple phenolic compounds.

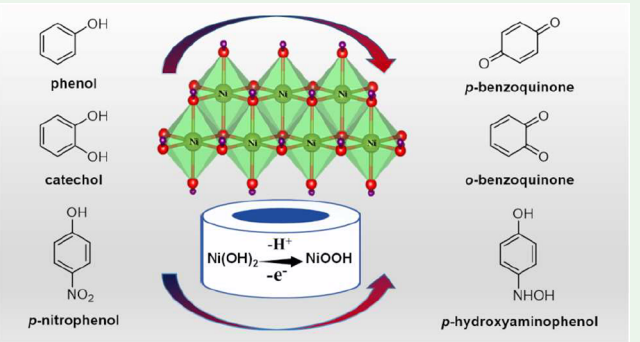

KEYWORDS: *electrochemical sensors, α-Ni(OH)$_2$, phenolic compounds, cyclic voltammetry, machine learning*

1. INTRODUCTION

Electrochemical sensors have emerged as powerful and promising devices for the detection of a broad range of gaseous and liquid-phase targets, owing to their low cost, portability, and rapid response. A key goal in advancing these technologies is the development of platforms capable of selectively detecting multiple analytes at distinct potentials, particularly for use in environmental monitoring, biomedical diagnostics, and quality control. However, this remains a significant challenge, especially in complex sample matrices, where signal interference and poor peak resolution can compromise sensor reliability and accuracy.

A particularly important class of environmentally and biologically relevant analytes is phenolic compounds (PCs), aromatic molecules containing one or more hydroxyl groups attached to a benzene ring. These compounds are widely used across various industrial sectors, including oil refining and petrochemical processing, pharmaceutical production, coking operations, resin manufacturing, and the fabrication of plastics, paints, pulp, paper, and wood products.[1−5] However, their amphiphilic nature enables them to act as protoplasmic poisons, allowing them to permeate cell membranes, denature proteins, and disrupt cellular function, inducing necrosis. These properties render many phenolic compounds toxic even at low concentrations.[6] Exposure to PCs above permissible levels poses serious health risks, prompting regulatory agencies such as the European Union (EU) and the United States Environmental Protection Agency (EPA) to designate most phenolic compounds as major environmental pollutants.[7] These organizations have set stringent maximum allowable concentrations for phenols and their derivatives in freshwater at 0.5 and 0.1 μg/L, respectively.[8] In comparison, the World Health Organization (WHO) and the Bureau of Indian Standards (BIS) prescribe a higher safety limit of 1 mg/L in drinking water.[9]

Given the harmful nature of phenolic compounds, there is an urgent need for reliable, rapid, and cost-effective detection

Received: August 11, 2025
Revised: October 4, 2025
Accepted: October 6, 2025
Published: October 10, 2025

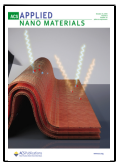

https://doi.org/10.1021/acsanm.5c03716
ACS Appl. Nano Mater. 2025, 8, 20463−20476

Scheme 1. Schematic Illustration of the Synthesis of α-Ni(OH)$_2$ via a Precipitation Route Using TEA in EtOH[a]

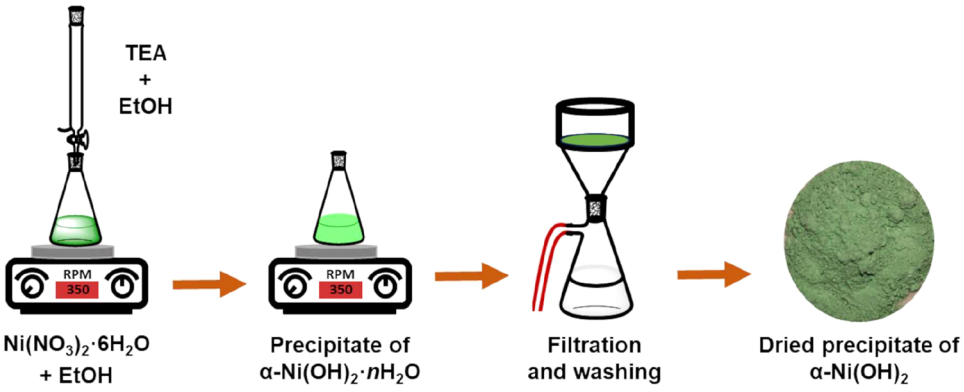

[a]The process involves the formation of a hydrated nickel hydroxide precipitate (α-Ni(OH)$_2$·nH$_2$O), followed by filtration, washing, and drying to afford α-Ni(OH)$_2$ powder.

strategies. Conventional analytical methods, such as spectrophotometry and chromatography, are highly sensitive and specific but are also expensive and labor-intensive, and require skilled personnel, which hinders their deployment in field settings.[10] Electrochemical sensors, by contrast, offer a compelling alternative due to their low cost, portability, real-time detection capabilities, and ease of automation.

To be practically useful, such sensors must exhibit high sensitivity, selectivity toward target analytes, and operational stability under ambient conditions to reduce maintenance and storage costs.[11] Among various sensor configurations, enzyme-based electrodes—especially those employing phenol oxidase or tyrosinase—have demonstrated promising results for detecting PCs. For instance, Park et al. developed a tyrosinase-based sensor that exhibited excellent sensitivity and selectivity.[12] Nevertheless, native enzyme-based sensors suffer several limitations, including high enzyme costs, poor long-term stability, and complex immobilization requirements necessary to preserve enzyme activity.[13]

To overcome these issues, recent efforts have focused on designing nonenzymatic electrochemical platforms that offer improved selectivity and stability for analyte detection. Materials investigated include carbon-based electrodes such as graphene, glassy carbon, and screen-printed carbon, as well as semiconductors such as zinc oxide and graphitic carbon nitride, which have shown considerable promise for detecting individual phenolic compounds.[14−17] For example, Maikap et al. reported catechol sensing using a ZnO-based electrode,[18] while Rajkumar et al. used sulfur-doped graphitic carbon nitride for *p*-nitrophenol detection.[19] Visagamani et al. demonstrated the use of a SrTiO$_3$/Ag/rGO-modified screen-printed electrode for selective sensing of *p*-nitrophenol.[20] Despite these advances, most existing systems are restricted to single-analyte detection. Reports of discrete sensors capable of selectively detecting multiple phenolic analytes through simple modulation of the applied potential are exceedingly rare.[21−23]

The present work demonstrates the development of a nonenzymatic sensing platform based on α-Ni(OH)$_2$, applied separately to a glassy carbon electrode (GCE) and a screen-printed carbon electrode (SPCE). These two formats enable the selective detection of trace amounts of phenol, catechol, and *p*-nitrophenol at distinct threshold potentials. We chose α-Ni(OH)$_2$ because its accessible Ni^{2+}/Ni^{3+} redox couple and layered nanoscale morphology promote adsorption and charge transfer during phenolic sensing (see Sections 3.1 and 3.2). Integrating α-Ni(OH)$_2$ into both conventional and portable sensing systems, and coupling this with data-driven signal modeling, provides a robust and versatile route to sensitive, selective, and portable detection of multiple phenolic compounds.

2. EXPERIMENTAL SECTION

2.1. Synthesis of α-Ni(OH)$_2$. Details on materials/reagents and phosphate-buffered saline (PBS) preparation are provided in the Supporting Information (SI). Following a literature-adapted coprecipitation protocol,[24] Ni(NO$_3$)$_2$·6H$_2$O (99.9%) was used as the precursor for synthesizing α-Ni(OH)$_2$. Triethylamine (TEA) and anhydrous ethanol (EtOH, 99.9%) were used as the precipitating agent and solvent, respectively. A 0.1 M nickel nitrate solution was prepared by dissolving the salt in ethanol. An ethanolic triethylamine solution (0.4 M) was added dropwise to the nickel nitrate solution in an Erlenmeyer flask at a controlled rate of 2 mL min^{-1}, with continuous stirring to obtain a precipitate (Scheme 1). The precipitate was separated by suction filtration, washed thoroughly with ethanol, and air-dried at ambient conditions for 24 h to afford α-Ni(OH)$_2$, which was used in all characterizations and electrochemical measurements reported here. In a separate control experiment, an aliquot of the dried solid was calcined at 600 °C in a muffle furnace to deliberately convert it to crystalline NiO. This confirmed that NiO forms only upon high-temperature treatment and is absent in the as-prepared precipitate. The resulting NiO exhibited poor sensing performance and was not pursued further.

2.2. Formation Behavior, Crystalline Nature, Microstructural Features, and Elemental Analyses of α-Ni(OH)$_2$. A variety of diagnostic tools—including FTIR, Raman, XRD, SEM, TEM, XPS—were employed to elucidate the phase formation, crystalline structure, microstructural features, and elemental composition of synthesized α-Ni(OH)$_2$. Structural and crystallinity analyses were performed using a Rigaku X-ray diffractometer with a Cu−Kα source at a scan rate of 5 degree/min over a 2θ range of 10−80°. Raman spectra were recorded using a Renishaw inVia micro-Raman spectrophotometer (UK) equipped with a 514.4 nm laser. The surface morphology of the nanoparticles was examined using a high-resolution transmission electron microscope (Talos F200 S, Thermo Fisher Scientific) and a field-emission scanning electron microscope (Apreo 2S, Thermo Fisher Scientific). Elemental composition and chemical state information were obtained via X-ray photoelectron spectroscopy (XPS) using a Thermo ESCALAB 250 instrument (Thermo Fisher Scientific). Fourier-transform infrared (FTIR) spectroscopy was performed using a Spectrum Two FTIR spectrometer (PerkinElmer) in the range of 400−4000 cm^{-1}. UV−vis spectroscopy was used to determine the band gap of the synthesized α-Ni(OH)$_2$ nanoparticles.

https://doi.org/10.1021/acsanm.5c03716
ACS Appl. Nano Mater. 2025, 8, 20463−20476

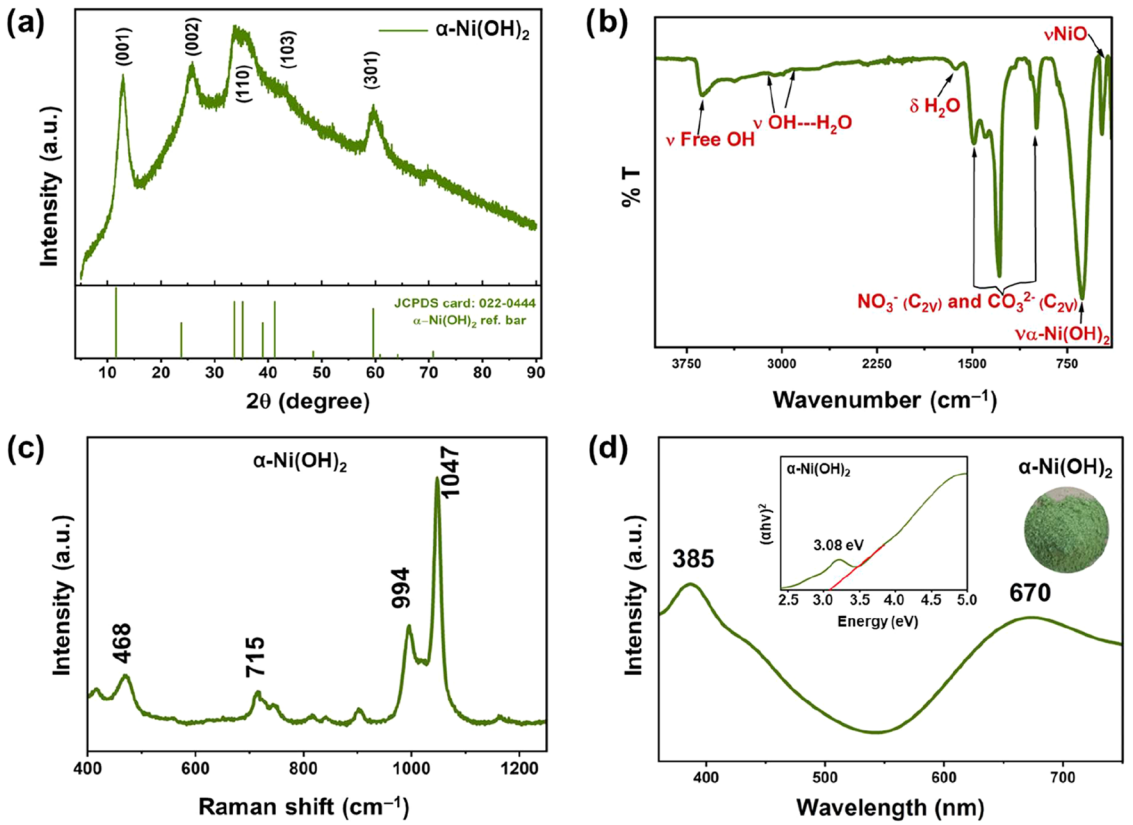

Figure 1. Characterization of α-Ni(OH)$_2$: (a) XRD pattern; (b) FTIR spectrum; (c) Raman spectrum; (d) UV−vis absorption spectrum. Insets in (d): Tauc plot and photograph of solid α-Ni(OH)$_2$.

2.3. Development of Working Electrode and SPCE for Electrochemical Sensing Studies. Electrochemical measurements were carried out using a standard three-electrode system consisting of a glassy carbon electrode (GCE, 3 mm diameter) as the working electrode , an Ag/AgCl reference electrode, and a platinum wire as the counter electrode. The GCE was mechanically polished using alumina slurries of decreasing particle size (1 μm, 0.3 μm, and 0.05 μm), followed by rinsing with EtOH and deionized (DI) water to remove surface impurities and ensure a clean, reproducible surface.

Ni(OH)$_2$ ink was prepared by dispersing 2 mg of Ni(OH)$_2$ powder in a mixture of 240 μL isopropyl alcohol (IPA), 160 μL DI water, and 15 μL Nafion (used as a binder), followed by 60 min of ultrasonication to obtain a homogeneous suspension. For electrode modification, 9 μL of this suspension was drop-cast onto the pretreated GCE surface and left to dry at room temperature. The SPCEs were cleaned by rinsing with EtOH and DI water, and 4 μL of the same Ni(OH)$_2$ suspension was drop-cast onto the working-electrode area. The electrodes were then air-dried under ambient conditions.

All electrochemical experiments were performed in 0.1 M PBS (pH 7), prepared with DI water. The pH value was selected based on preliminary studies, which identified it as the optimal condition for achieving the highest electrochemical response, while also reflecting environmentally relevant conditions (see Figure S1 in the SI). Cyclic voltammetry (CV) and amperometric measurements were performed at room temperature using a Metrohm Autolab VIONIC electrochemical workstation (Potentiostat 1, Switzerland) controlled by INTELLO software. In CV analysis, the anodic peak current (I_{pa}) corresponds to oxidation processes, while the cathodic peak current (I_{pc}) corresponds to reduction processes. CV was used to determine the threshold potentials for phenol, catechol, and *p*-nitrophenol, which were subsequently applied in amperometric measurements to monitor current responses and determine limits of detection (LODs) for both the GCE and SPCE platforms.

2.4. Machine Learning Implementation. Machine learning (ML) techniques were employed to classify the analyte type based on data collected from two independent electrochemical platforms: (i) GCE and (ii) SPCE. The data sets used for model training and evaluation comprised 11,500 records for the GCE configuration and 12,000 for the SPCE configuration. These records were generated through systematic CV measurements. Each record corresponded to a single measurement and included three input features: applied potential, measured current, and analyte concentration. The classification target was the analyte type: phenol, catechol, or *p*-nitrophenol.

To ensure robust analyte classification, four well-established supervised learning algorithms were implemented: logistic regression,[25] random forest,[26−28] k-nearest neighbors (KNN),[29] and support vector machines (SVMs).[30,31] Logistic regression, suited for both binary and multiclass classification, was trained on the input features to distinguish between the three analytes. Random forest was selected for its ability to handle nonlinear relationships and high-dimensional data, making it particularly effective for complex sensor outputs. The KNN algorithm, a nonparametric, instance-based learning method, classifies data points based on the majority class among their nearest neighbors in feature space. Finally, SVM was employed to construct optimal decision boundaries (hyperplanes) that maximize separation between classes, using a radial basis function (RBF) kernel.

Model performance was evaluated using standard classification metrics, including accuracy, precision, recall, and F1-score.[32−34] These metrics enabled a quantitative comparison of predictive performance across algorithms and provided a deeper understanding of the relationship between electrochemical signals and analyte type. The complete data processing and modeling workflow is summarized in Scheme S1 in the SI.

https://doi.org/10.1021/acsanm.5c03716
ACS Appl. Nano Mater. 2025, 8, 20463−20476

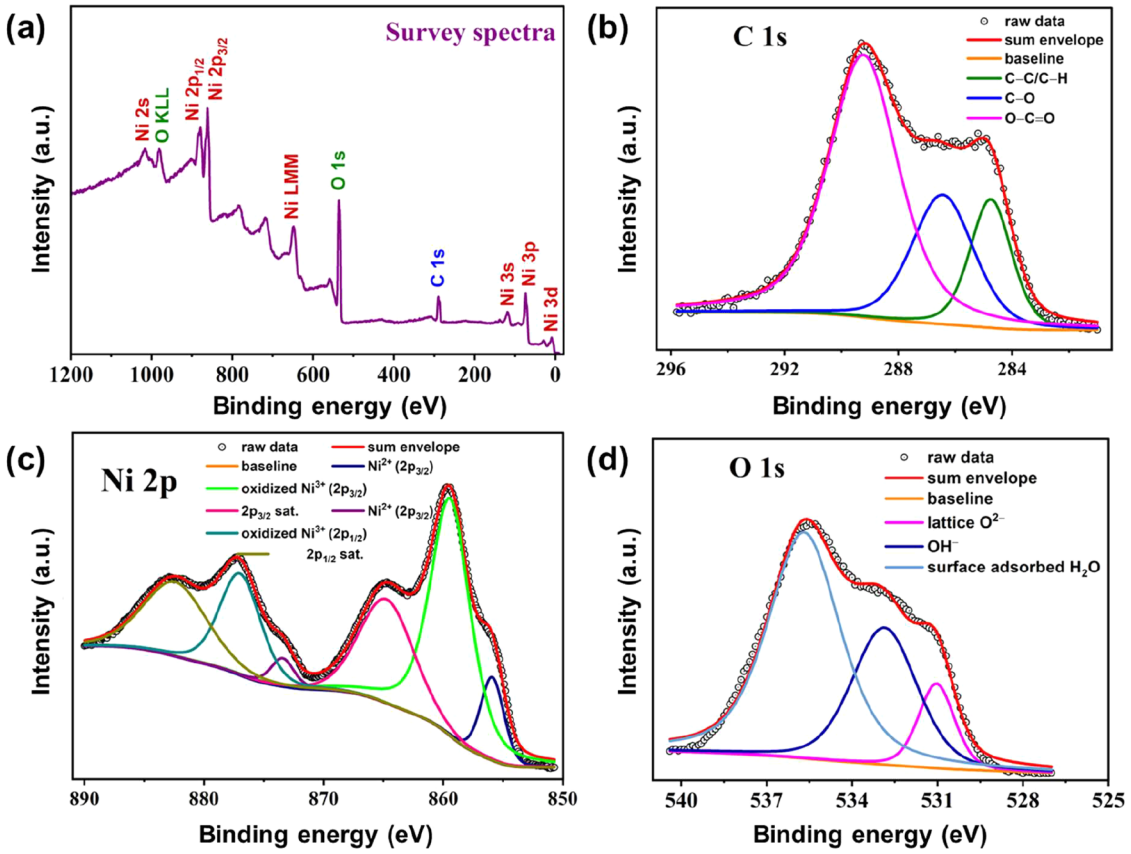

Figure 2. (a) XPS survey spectrum of α-Ni(OH)$_2$; high resolution, peak-fitted XPS spectra of (b) C 1s, (c) Ni 2p, and (d) O 1s.

3. RESULTS AND DISCUSSION

3.1. Structural and Spectroscopic Characterization of α-Ni(OH)$_2$. The XRD pattern of Ni(OH)$_2$ powder, shown in Figure 1(a), displays distinct diffraction peaks at 2θ = 12, 25.4, 33.4, and 59.4°, corresponding to its (001), (002), (110), and (300) lattice planes, consistent with JCPDS 22−0444 and confirming that the synthesized Ni(OH)$_2$ crystallizes in its α-polymorph. The α-Ni(OH)$_2$ phase consists of β-Ni(OH)$_2$ layers oriented parallel to the crystallographic ab-plane and intercalated with water molecules, with the hydration level varying between $0.41 \leq x \leq 0.7$. The diffraction angles for the (001) and (002) lattice planes are slightly larger than those listed in the standard JCPDS card for α-Ni(OH)$_2$. In our PXRD pattern, positive peak shifts are observed due to the intercalation of anions and water molecules into the interlayer spaces. Such intercalation leads to disordered stacking of the nickel hydroxide sheets, imparting a turbostratic character to α-Ni(OH)$_2$ and resulting in broad, weak, and diffuse halo-like diffraction peaks. This disorder stacking stems from weak interactions between intercalated anions, which lead to random orientations and the absence of long-range crystallographic order.[35] Additionally, the interlayer region frequently incorporates residual anions from the Ni(II) salt used during sample preparation.[36] This turbostratic, semicrystalline nanostructure increases the density of edge/defect sites and accessible Ni centers with shortens ion/electron diffusion paths, which collectively enhance adsorption and charge transfer during sensing. Moreover, the asymmetric peak around 2θ = 33.4° indicates the presence of a turbostratic α-Ni(OH)$_2$ phase, which arises from the disordered stacking of nickel hydroxide sheets due to these intercalated species. An interlayer spacing estimated at 0.7−0.9 nm further reflects the structural arrangement influenced by the intercalated anions.[37]

The FTIR spectrum of α-Ni(OH)$_2$, shown in Figure 1(b), is characterized by distinct vibrational features. A prominent peak at approximately 3615 cm^{-1} corresponds to the O−H stretching vibration within the α-Ni(OH)$_2$ lattice. A broad band observed between 3500−3550 cm^{-1} is attributed to the O−H stretching of free water molecules, while a band around 1630 cm^{-1} corresponds to the bending vibration of these water molecules.[38] Furthermore, bands near 1493, 1396, 1288, 1041, and 989 cm^{-1} are associated with the presence of intercalated nitrate arising from the precursor salt.[37] The Ni−O lattice vibration of α-Ni(OH)$_2$ is represented by a band near 635 cm^{-1}.[39,40]

Figure 1(c) shows the Raman spectrum of α-Ni(OH)$_2$. In the free state, nitrate ions typically exhibit D_{3h} symmetry with four characteristic vibrational modes: ν_1 at 1050 cm^{-1} (A_1', IR-inactive), ν_2 at 831 cm^{-1} (A_2'', Raman-inactive), ν_3 at 1390 cm^{-1} (E'), and ν_4 at 720 cm^{-1} (E').[41] In the present spectrum, the most prominent feature is the ν_1 mode observed at 1043 cm^{-1}, indicative of nitrate groups present within the α-Ni(OH)$_2$ lattice. The vibrational patterns are very similar to those of nickel salts and anion-intercalated α-Ni(OH)$_2$; for instance, nitrate-intercalated α-Ni(OH)$_2$ materials are closely related to nickel hydroxy nitrate (NHN) compounds, with NHN exhibiting a distinct peak at 990 cm^{-1} that accounts for the observed feature at 996 cm^{-1} even in the absence of free nitrate ions.[42] Additionally, two vibrational bands observed at 470 and 717 cm^{-1} appear to couple anharmonically, giving rise to a combination band at 1625 cm^{-1}.[41] These spectral lines

https://doi.org/10.1021/acsanm.5c03716
ACS Appl. Nano Mater. 2025, 8, 20463−20476

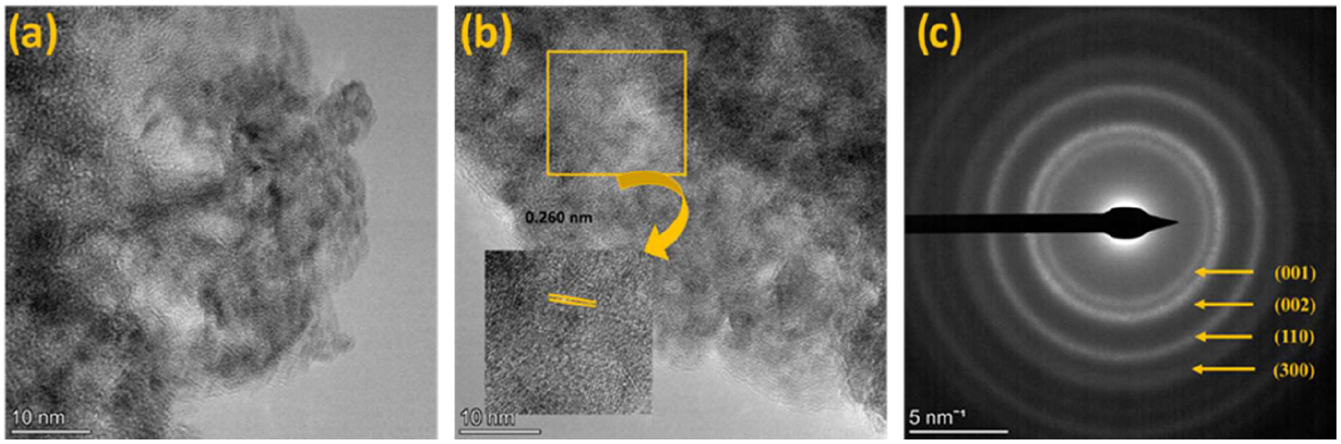

Figure 3. (a,b) High-resolution TEM images of α-Ni(OH)$_2$; (c) SAED pattern of α-Ni(OH)$_2$ nanoparticles.

feature the complex interplay between the vibrational modes of the lattice and the intercalated anions.

Figure 1(d) presents the UV−vis absorption spectrum of α-Ni(OH)$_2$ powders, revealing two distinct peaks at 385 and 670 nm that are attributed to the d-d transitions of Ni^{2+} cations.[43] The inset in Figure 1(d) shows the Tauc plot of $(\alpha h\nu)^2$ versus energy (eV) derived from the absorption data. The optical band gap energy of the α-Ni(OH)$_2$ powder is determined to be 3.08 eV.

The chemical states of α-Ni(OH)$_2$ were investigated by XPS to assess the oxidation states of Ni and related surface species. As shown in Figure 2(a), the XPS survey spectrum of α-Ni(OH)$_2$ reveals the presence of Ni, O, and C, with the C 1s signal at ∼284.8 eV arising from adventitious carbon contamination. This peak was used to calibrate the binding energies of other elements and to correct for charging effects, as it does not contribute to the intrinsic chemical states of the sample elements. All high-resolution XPS (HP-XPS) spectra, including Ni 2p, O 1s, and C 1s, were deconvoluted using the XPSPeak41 software, applying a linear combination of Gaussian−Lorentzian (SGL) line shapes with a Shirley-type function for background correction. The C 1s spectrum (Figure 2(b)) was fit with three components at 284.78, 286.44, and 289.23 eV, corresponding to C−C/C−H (adventitious hydrocarbons), C−O, and O−C═O groups, respectively. The broadening and increased intensity of the higher binding-energy peaks are attributed to the adsorption of CO and CO_2 upon air exposure.[44]

The Ni 2p spectrum (Figure 2(c)) shows two primary peaks at 855.89 eV ($2p_{3/2}$) and 873.42 eV ($2p_{1/2}$), consistent with Ni^{2+} in α-Ni(OH)$_2$, with a spin−orbit splitting of 17.53 eV. Corresponding shakeup satellite peaks are observed at 864.75 and 882.42 eV. Additional intense peaks at 859.41 eV ($2p_{3/2}$) and 876.99 eV ($2p_{1/2}$) indicate the presence of oxidized Ni^{3+} species. These are likely associated with surface NiOOH formation, resulting from electron-withdrawing effects induced by oxygenated carbon species during XPS measurements.[45,46]

The O 1s spectrum (Figure 2(d)) displays peaks at 531.04, 532.86, and 535.69 eV, which correspond to lattice O^{2-} in α-Ni(OH)$_2$, OH^- species from surface oxidation, and surface-adsorbed water molecules, respectively. The higher binding energies observed are attributed to electron-withdrawing interactions at the Ni centers, which increase their affinity for OH^- adsorption.[46]

The microstructural and crystallographic characteristics of α-Ni(OH)$_2$ were further investigated by transmission electron microscopy (TEM). As shown in Figure 3(a,b), high-resolution TEM images reveal semicrystalline particles with clear lattice fringes; the measured d-spacing of 2.60 Å corresponds to the (110) planes of α-Ni(OH)$_2$ (Figure 3(b)). The selected-area electron diffraction (SAED) pattern (Figure 3(c)) confirms the polycrystalline nature of the material. Complementary field-emission scanning electron microscopy (FESEM) analysis provided a particle-size distribution with an average α-Ni(OH)$_2$ particle size of ∼100 nm (Figure S2 in the SI).

3.2. Electrochemical Performance of α-Ni(OH)$_2$/GCE.

The electrochemical sensing capability of the developed α-Ni(OH)$_2$/GCE electrode was first assessed using catechol as a model analyte in a three-electrode setup. Catechol was chosen because it undergoes a well-defined, reversible redox process (catechol/o-quinone), giving both anodic (I_{pa}) and cathodic (I_{pc}) peak currents that provide a clear benchmark for evaluating electron-transfer behavior. As shown in Figure 4(a), the CV response varies with the scan rate. Increasing the scan rate from 10 to 150 mV s^{-1} resulted in higher I_{pa} values and a shift in peak potential toward more positive values. The relationship between peak current and scan rate (Figure 4b) gave R^2 = 0.9016 (I_{pa}) and 0.9746 (I_{pc}), whereas plotting against the square root of scan rate (Figure 4c) yielded stronger linearities of R^2 = 0.9700 (I_{pa}) and 0.9849 (I_{pc}). These results confirm that the redox process is predominantly diffusion-controlled, consistent with the Randles−Ševčík model.

To ensure consistency in subsequent analyses, a scan rate of 50 mV s^{-1} was selected for all further concentration-dependent measurements.

Figure 5(a) shows the CV responses of the developed working electrode with increasing concentrations of phenol. As illustrated in Figure 5(b), the anodic peak current increases linearly with phenol concentration in the range of 0.3−10 μM. During this process, a single irreversible oxidation peak appears at approximately 0.72 V in the anodic region, likely resulting from the adsorption and subsequent oxidation of phenoxide anions (PhO^-) on the electrode surface. Under alkaline/near-surface basic conditions, phenol is deprotonated to PhO^-, which undergoes one-electron oxidation to generate a phenoxy radical. These radicals may undergo follow-up reactions, including with surface-bound hydroxyl species, forming

https://doi.org/10.1021/acsanm.5c03716
ACS Appl. Nano Mater. 2025, 8, 20463−20476

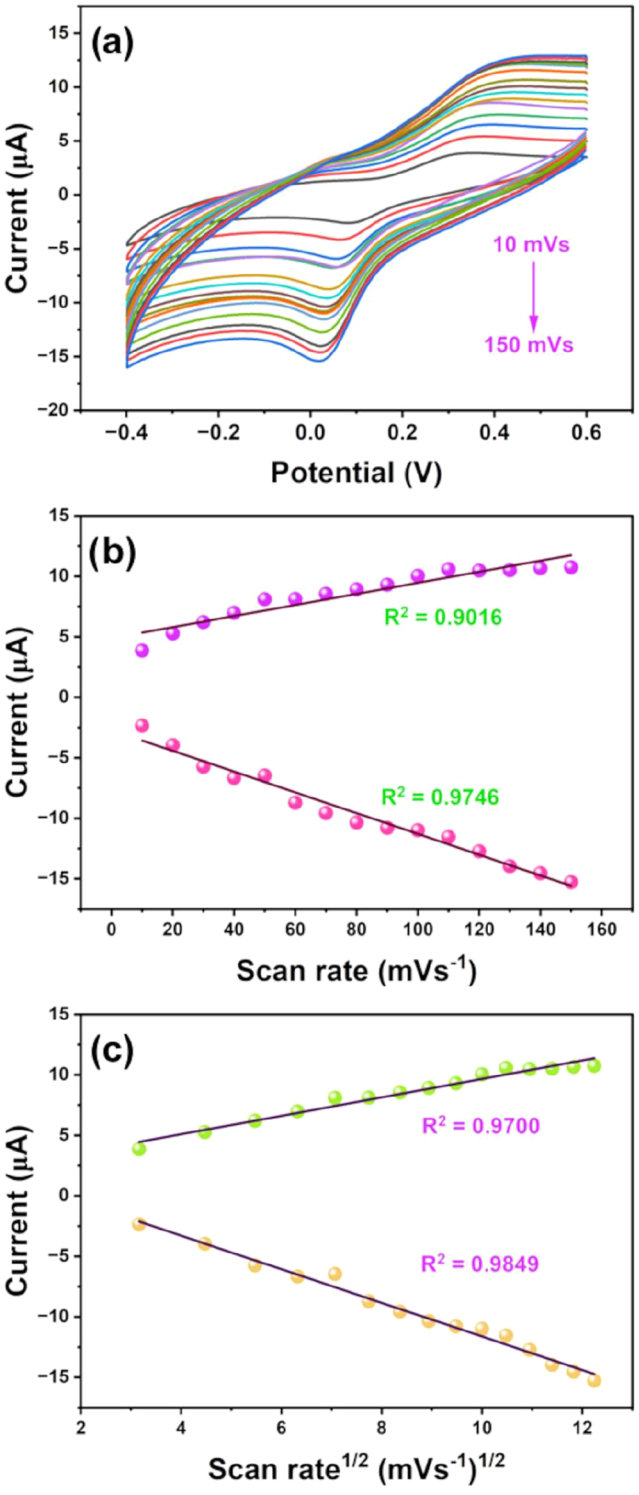

Figure 4. (a) CVs of 150 μM catechol in 0.1 M PBS at varying scan rates using the α-Ni(OH)$_2$/GCE; (b) anodic (I_{pa}) and cathodic (I_{pc}) peak currents vs scan rate; (c) I_{pa} and I_{pc} vs scan rate$^{1/2}$.

hydroquinone-like intermediates. Hydroquinone is then electrochemically oxidized in a two-electron process to yield *p*-benzoquinone (see Scheme 2).

The developed electrode also demonstrated effective sensing capability for catechol and *p*-nitrophenol. Figure 5(c) presents the CVs recorded for catechol over 10−150 μM. Both anodic (I_{pa}) and cathodic (I_{pc}) peaks are observed, consistent with the reversible catechol/*o*-benzoquinone couple. The corresponding linear dependence of peak currents on concentration is shown in Figure 5(d). For calibration and LOD determination we used the anodic peak, which afforded slightly better linearity (R^2 = 0.9947 vs 0.9868 for I_{pc}) and more reproducible signals across the tested range.

For *p*-nitrophenol, CVs recorded over 20−180 μM are shown in Figure 5(e). The corresponding linear increase in peak current with concentration is presented in Figure 5(f), confirming the electrode's sensitivity toward this analyte as well. Among the three analytes, phenol exhibits the strongest electrochemical response, with a linear current−concentration relationship extending to submicromolar levels. While the precise LOD for phenol is discussed in Section 3.4, these CV results already point to its superior detectability compared to catechol and *p*-nitrophenol. Based on the calibration plots in Figure 5, the LODs for catechol and *p*-nitrophenol were estimated to be 0.1 and 1 μM, respectively.

The observed cathodic peak for *p*-nitrophenol is attributed to an irreversible electrochemical reduction process. This is proposed to proceed via a four-electron/four-proton ($4e^-$, $4H^+$) transfer pathway, resulting in the formation of *p*-hydroxyaminophenol as the principal product.[19] Such multielectron reduction mechanisms are typical for nitroaromatic compounds and reflect the sensor's ability to mediate complex redox transformations.[47]

The α-Ni(OH)$_2$/GCE electrode demonstrates excellent performance for detecting phenolic compounds, largely due to the redox activity of nickel species on its surface. A key step in the sensing mechanism is the electrochemical oxidation of Ni^{2+} to Ni^{3+}, which leads to the *in situ* formation of NiOOH. This NiOOH phase functions as a strong oxidizing agent that facilitates the indirect oxidation of phenolic analytes. In this mediated process, phenolic molecules adsorb onto the electrode surface and are oxidized by Ni^{3+} species, while NiOOH is simultaneously reduced back to Ni(OH)$_2$. This reversible Ni^{2+}/Ni^{3+} redox cycle enhances electrocatalytic activity and enables continuous sensing of phenolic compounds. Additionally, interactions between phenolic molecules and surface hydroxyl groups further support adsorption and electron transfer. As a result, the α-Ni(OH)$_2$/GCE electrode can effectively detect multiple phenolic analytes at distinct oxidation potentials. The overall transformation of α-Ni(OH)$_2$ to NiOOH and the corresponding oxidation of the target compounds are illustrated in Scheme 2. Consistent with this mechanism, anodic polarization produces a thin NiOOH-like surface layer (Ni^{2+}/Ni^{3+} couple),[43,45,46] as suggested by our CV features and the Ni^{3+} components observed by XPS on the postsensing electrode material. Complementary postsensing PXRD and XPS analyses confirm a slight transformation of Ni(OH)$_2$ into NiOOH during sensing, as shown in Figures S3 and S4, respectively.

3.3. Electrochemical Performance of α-Ni(OH)$_2$/SPCE.

Sensitive detection of phenol, catechol, and *p*-nitrophenol was also achieved using the α-Ni(OH)$_2$/SPCE platform. The CV responses of the developed SPCE in the presence of each analyte, along with corresponding peak current variations as a function of concentration, are presented in Figure 6.

Figure 6(a) shows the CV profiles recorded for phenol over 10−150 μM. The linear fit of the anodic peak current with phenol concentration is shown in Figure 6(b), with a clear linear dependence observed between 50 and 150 μM. Similar to the GCE system, the SPCE also exhibits both anodic and

https://doi.org/10.1021/acsanm.5c03716
ACS Appl. Nano Mater. 2025, 8, 20463−20476

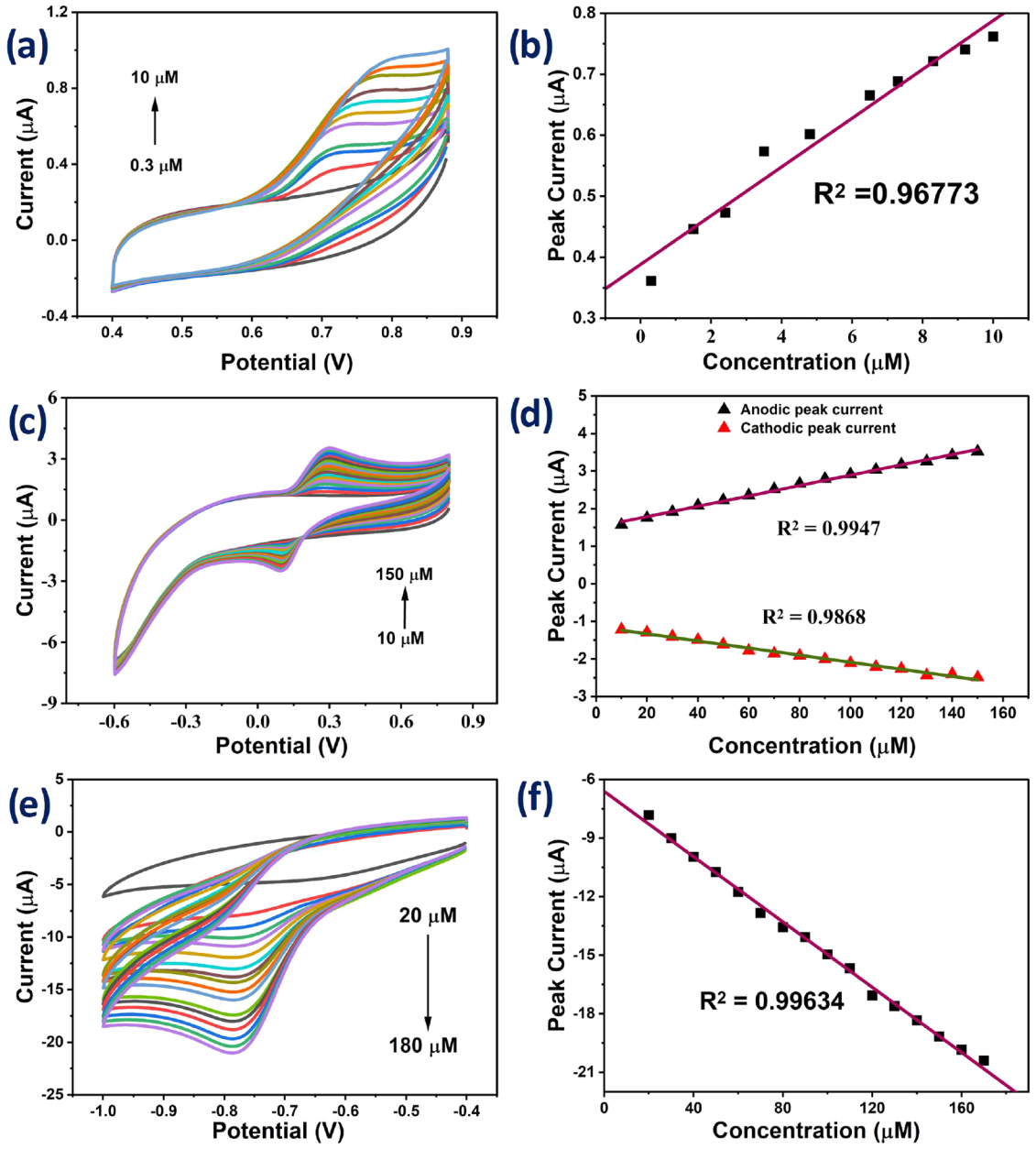

Figure 5. (a) CVs of phenol at α-Ni(OH)$_2$/GCE over 0.3−10 μM; (b) corresponding anodic peak current (I_{pa}) vs concentration (used for calibration/LOD). (c) CVs of catechol at α-Ni(OH)$_2$/GCE over 10−150 μM showing both anodic (I_{pa}) and cathodic (I_{pc}) peaks; (d) I_{pa} and I_{pc} vs concentration (I_{pa} used for calibration/LOD due to slightly better linearity and reproducibility). (e) CVs of *p*-nitrophenol at α-Ni(OH)$_2$/GCE over 20−180 μM; (f) corresponding cathodic peak current (I_{pc}) vs concentration (used for calibration/LOD).

cathodic peaks for catechol detection (Figure 6(c)). The peak currents for both redox processes increase linearly with catechol concentration over 20−250 μM, as illustrated in Figure 6(d).

Finally, the CV responses for *p*-nitrophenol at varying concentrations are shown in Figure 6(e), and the corresponding linear relationship between peak current and analyte concentration is presented in Figure 6(f), confirming the SPCE's suitability for detecting all three phenolic compounds. Based on these concentration-dependent responses, the LODs for the α-Ni(OH)$_2$/SPCE sensor were estimated to be 0.3 μM for phenol, 1 μM for catechol, and 2 μM for *p*-nitrophenol.

It is notable that the peak positions for phenolic analyte detection differ between the GCE and SPCE systems, despite both being modified with the same α-Ni(OH)$_2$ paste. The shifts observed in CV—with GCE typically exhibiting less positive peak potentials—can be attributed to variations in electron-transfer kinetics and diffusion with each electrode type. Electrodes with slower electron-transfer kinetics generally require higher overpotentials to facilitate the redox reactions, resulting in more positive or shifted peak positions. Additionally, differences in diffusion influence the rate at which analytes reach the electrode surface: slower diffusion can lead to broader, less defined peaks and potential shifts due to mass-transport limitations, whereas faster diffusion tends to produce sharper peaks closer to the formal redox potential. These combined effects contribute to the electrode-dependent differences in electrochemical response observed in this study.

It is worth noting that the SPCE's lower current response relative to the three-electrode GCE setup is expected, reflecting

https://doi.org/10.1021/acsanm.5c03716
ACS Appl. Nano Mater. 2025, 8, 20463−20476

Scheme 2. Schematic Representation of the Electrochemical Transformation of Phenolic Compounds at the α-Ni(OH)$_2$/GCE

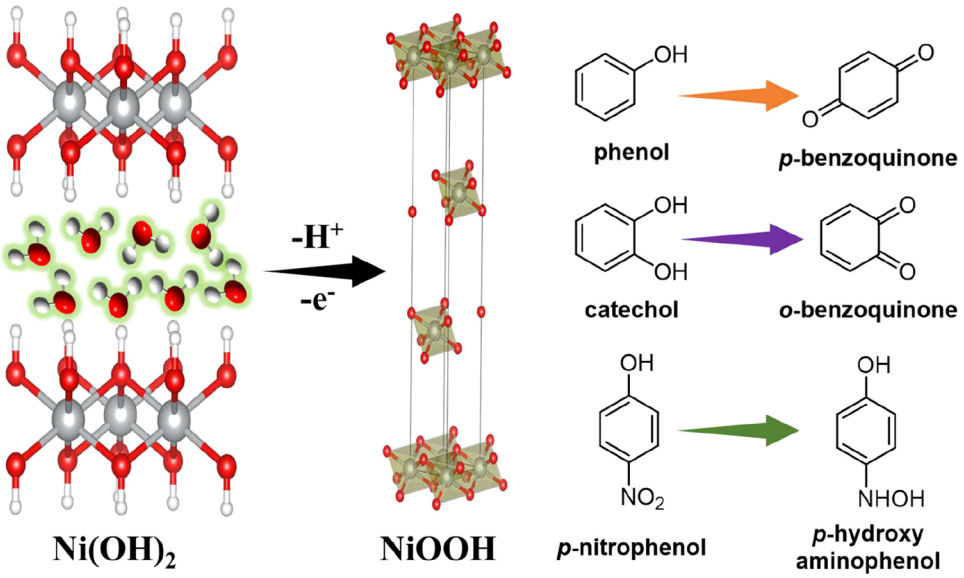

its miniaturized active area, reduced mass transport in drop-cell configurations, and the use of a pseudoreference electrode that can modestly affect peak positions and reproducibility.

As shown in Figure S5 in the SI, the detection peaks for phenol, catechol, and *p*-nitrophenol appear at distinct potentials on both the GCE and SPCE platforms. However, for each analyte, the peak potentials differ between the two electrodes. The observed potential shifts between GCE and SPCE follow a descending trend in the order phenol > catechol > *p*-nitrophenol. CV studies further demonstrate that both platforms exhibit the highest sensitivity toward phenol, followed by catechol and *p*-nitrophenol.

3.4. Amperometric Analysis for Trace-Level Detection. To further assess the sensor performance, amperometric measurements were carried out using the α-Ni(OH)$_2$/GCE in 0.1 M PBS (pH 7). Phenol concentrations were varied over a broad range to evaluate the electrode's response under low and moderate analyte levels. Figure 7(a,b) display the amperometric responses obtained for phenol over 0.03−0.24 μM and 0.3−2.5 μM, respectively. In both ranges, the α-Ni(OH)$_2$-modified GCE exhibited consistent and accurate detection.

The calibration curve in Figure 7(c) shows the relationship between the current change relative to baseline and phenol concentration. A strong linear correlation was observed across the tested range (R^2 = 0.9804), confirming the precision and reliability of the electrode. However, slight deviations from linearity were noted at the lowest concentrations, for which a separate linear fit provided a better approximation. To complement these results, amperometric measurements were also conducted for catechol and *p*-nitrophenol at their respective optimized detection potentials (+0.33 V and −0.77 V, vs Ag/AgCl), in addition to phenol at +0.72 V. As shown in Figure S6 in the SI, the α-Ni(OH)$_2$/GCE electrode exhibited stable and sensitive responses for both analytes, confirming its broader applicability beyond phenol. From the low-concentration amperometric measurements, the LOD for phenol was 0.003 μM, highlighting the exceptional sensitivity of the α-Ni(OH)$_2$/GCE system for trace phenol quantification. These detection limits (0.003 μM for phenol, 0.1 μM for catechol, and 1 μM for *p*-nitrophenol on GCE; 0.3, 1, and 2 μM on SPCE, respectively) compare favorably with Ni-based and related phenolic sensors reported in the literature. A side-by-side benchmark is provided in Table 1, which shows that the present α-Ni(OH)$_2$ electrodes deliver competitive or superior sensitivities across the three analytes while offering the added advantage of a single platform that detects multiple phenolic species at distinct potentials.

In addition to LODs, the sensitivities (slope of current vs concentration) were 3.99 × 10^{-8} A μM^{-1} for the α-Ni(OH)$_2$/GCE and 1.29 × 10^{-8} A μM^{-1} for the α-Ni(OH)$_2$/SPCE (Figure S7 in the SI). The higher GCE sensitivity reflects both a larger electroactive area and faster electron-transfer kinetics relative to SPCE.

Finally, selectivity under amperometric conditions was evaluated at the catechol working potential (+0.33 V vs Ag/AgCl) by interleaving injections of catechol with common electroactive species (glucose, *p*-nitrophenol, phenol, H_2O_2, NO_2^-) in 0.1 M PBS (pH 7). As shown in Figure S8 in the SI, only catechol produced distinct current steps at +0.33 V, whereas the interferents were negligible at this potential (consistent with their redox activity occurring at +0.72 V for phenol and −0.77 V for *p*-nitrophenol). These results confirm operational selectivity via potential-resolved detection in our α-Ni(OH)$_2$/GCE platform.

3.5. Machine Learning Implementation and Analysis. In this section, we apply ML techniques to classify electrochemical signals corresponding to phenol, catechol, and *p*-nitrophenol. We evaluated four widely used supervised learning models: logistic regression (LR), random forest (RF), support vector machine (SVM), and k-nearest neighbors (KNN), using two data sets derived from the GCE and SPCE platforms (see Section 2.4 for details).

Across both data sets, LR, RF, and KNN achieved perfect classification metrics, with accuracy, precision, recall, F1-score, and the area under the receiver operating characteristic (ROC) curve (AUC) all equal to 1.0. These models showed zero standard deviation in cross-validated F1 scores, indicating remarkable stability and generalization across folds. The classification performance for the GCE and SPCE data sets is summarized in Figures 8 and S9 in the SI, respectively. In

https://doi.org/10.1021/acsanm.5c03716
ACS Appl. Nano Mater. 2025, 8, 20463−20476

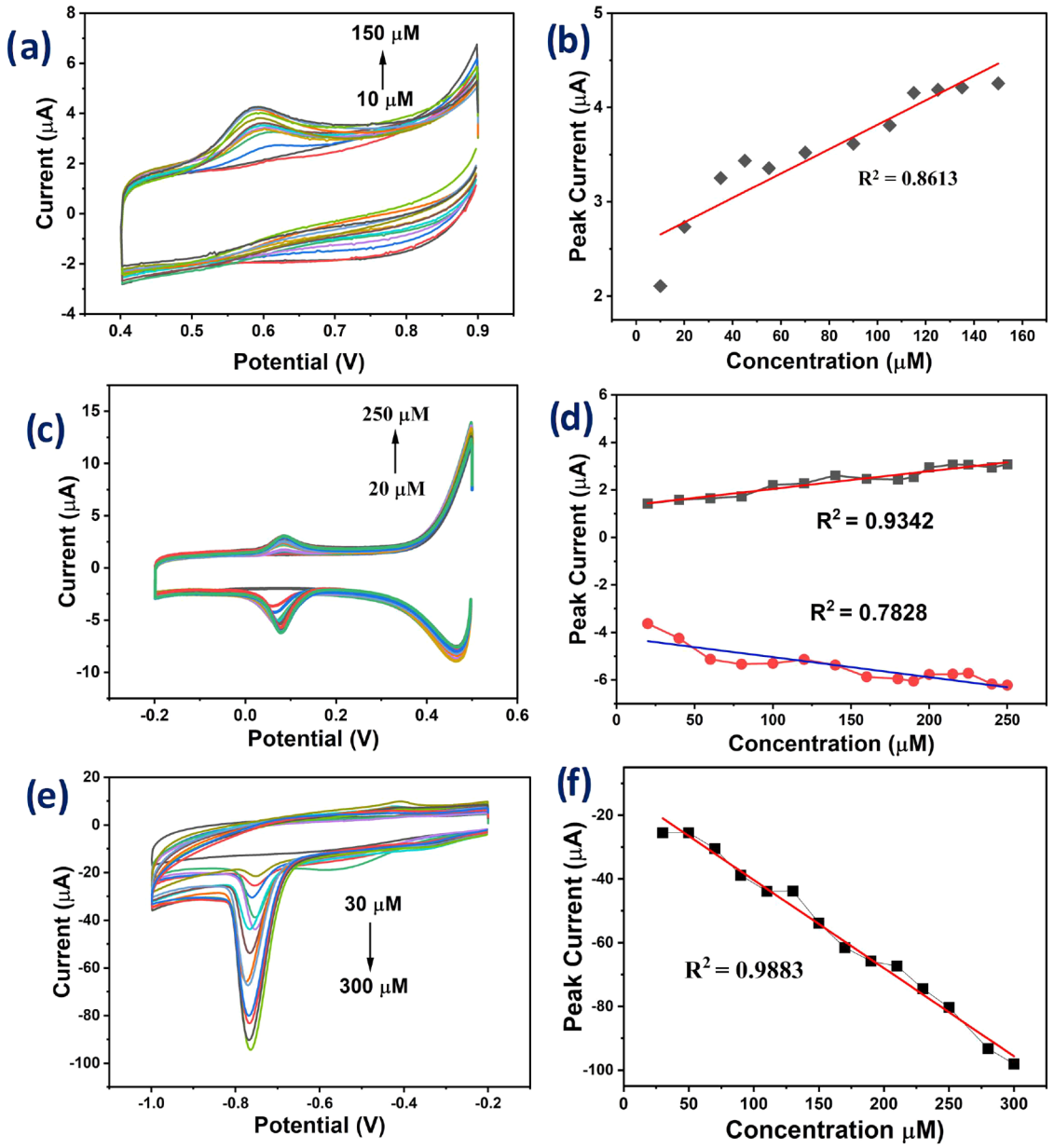

Figure 6. Electrochemical response of α-Ni(OH)$_2$/SPCE toward phenolic compounds: (a) CVs for phenol over 10−150 μM; (b) corresponding anodic peak current (I_{pa}) vs concentration (used for calibration/LOD). (c) CVs for catechol over 20−250 μM showing both anodic (I_{pa}) and cathodic (I_{pc}) peaks; (d) I_{pa} and I_{pc} vs concentration (I_{pa} used for calibration/LOD, owing to better linearity/reproducibility). (e) CVs for *p*-nitrophenol over 30−300 μM; (f) corresponding cathodic peak current (I_{pc}) vs concentration (used for calibration/LOD).

both figures, the confusion matrices (panels a) were generated from out-of-fold test predictions obtained during 5-fold cross-validation; rows correspond to the true analyte class and columns to the predicted class.

As shown in Figure 8(a), the strong performance of the RF model likely stems from its capability to handle complex, nonlinear interactions within the data, as well as its robustness against overfitting. LR also achieved perfect classification, benefiting from the clear linear separability present in the feature space. The KNN model likewise achieved flawless performance; however, because it is instance-based, it can be sensitive to noise and feature scaling, so careful choice of k and distance metric is important to avoid overfitting.

In contrast, SVM showed comparatively lower performance, with an accuracy of 78.18% and an ROC AUC value of 0.89, as shown in Figure 8(b). This reduced performance may be attributed to limitations in capturing nonlinear boundaries, potentially due to a suboptimal kernel or untuned hyperparameters.

To assess model robustness and minimize overfitting, a 5-fold cross-validation strategy was employed, with results summarized in Figure 8(c). Both LR and RF maintained consistent performance across all folds, confirming their reliability. While KNN achieved perfect classification scores, its variation across folds reinforces concerns regarding potential overfitting. SVM exhibited moderate fluctuations, highlighting its sensitivity to data partitioning and the importance of careful kernel selection and tuning.

A similar evaluation was performed using SPCE-derived CV data for the classification of the analytes studied. As shown in

https://doi.org/10.1021/acsanm.5c03716
ACS Appl. Nano Mater. 2025, 8, 20463−20476

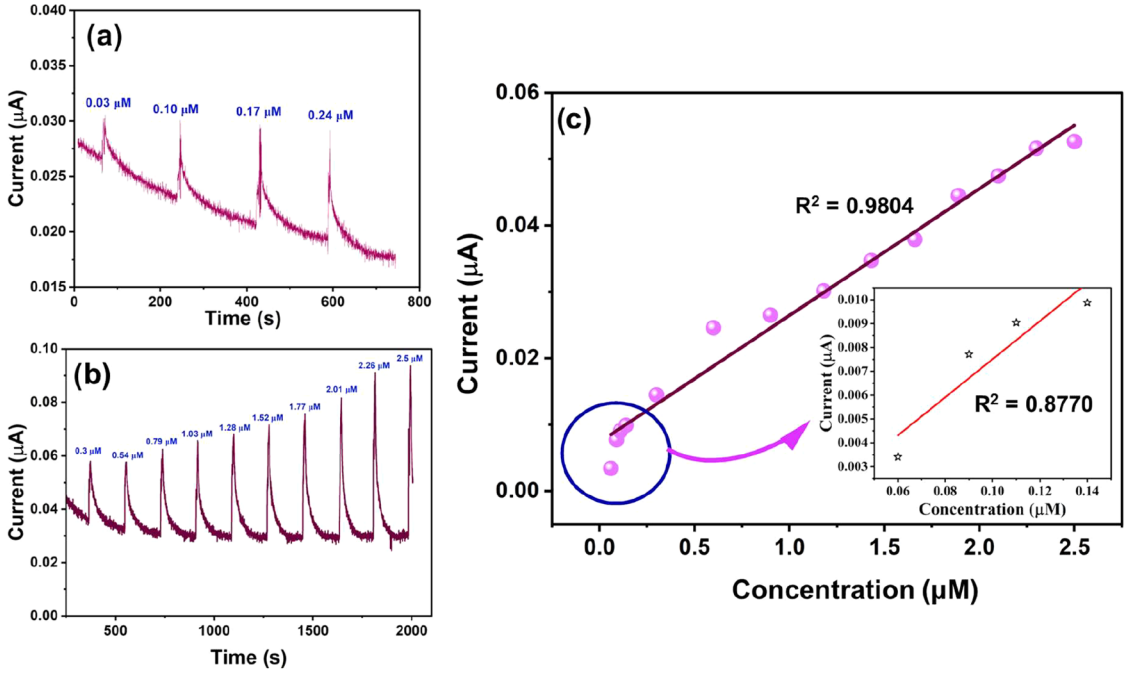

Figure 7. Amperometric response of the α-Ni(OH)$_2$/GCE for phenol detection: (a) current responses for 0.03−0.24 μM phenol; (b) responses for 0.3−2.5 μM phenol; (c) calibration curve showing the dependence of peak current on phenol concentration over 0.06−2.5 μM. Inset: linear fit for the low-concentration range 0.06−0.34 μM.

Table 1. Comparison of Electrochemical Analytical Parameters for Modified α-Ni(OH)$_2$/GCE and α-Ni(OH)$_2$/SPCE Sensors (This Work) versus Representative Literature Reports

sensor material/electrode	analyte	LOD (μM)	reference
Ni/Co pyrophosphate nanosheets	phenol	0.25	48
NiAl-LDH nanoflowers/GCE	phenol	0.02	49
Ni-doped BaO nanoclusters	phenol	0.03	50
ZnO/Ag-CeO$_2$ nanocomposite/GCE	phenol	0.021	51
Gd/NiO hollow microspheres/GC	phenol	0.076	52
gold nanoparticles/chitosan@N,S Co-doped MWCNT	catechol	0.006	53
Bi$_2$O$_3$@RGO/screen printed carbon electrode	catechol	0.015	54
MnO$_2$ nanosheets on reduced graphene oxide (rGO)	catechol	0.008	55
MtPcCo/ErGO	catechol	0.53	56
CBO/GR-15	catechol	0.0004	57
S-GCN/SPCE	*p*-NP	0.0016	19
AgNWs@PANIb/GCE	*p*-NP	0.052	58
Cu-Curcc/GCE	*p*-NP	0.682	59
SrTiO$_3$/Ag/rGO	*p*-NP	0.03	20
APL/GCE	*p*-NP	0.0096	60
α-Ni(OH)$_2$/GCE	phenol	0.003	this work
	catechol	0.1	
	p-NP	1.00	
α-Ni(OH)$_2$/SPCE	phenol	0.3	
	catechol	1.00	
	p-NP	2.00	

Figure S9 in the SI, LR, RF, and KNN achieved perfect classification scores. Figure 8(a) illustrates the variations of confusion matrices for LR and SVM.

While SVM produced consistently poor classification results—evidenced by a minuscule cross-validated F1 standard deviation of 0.0002—this consistency underscores the need for kernel-specific optimization to better handle overlapping classes (Figure S9(b)). Despite a high average ROC AUC of 0.991, SVM performed poorly on core classification metrics, with accuracy = 52%, precision = 0.27, and F1-score = 0.35 (Figure S9(c)). This discrepancy between high AUC and low classification accuracy suggests that, although SVM ranked class probabilities effectively, its decision boundary was misaligned with the true class distributions, as further supported by the t-SNE representation in Figure S9(d).

Further insights into model performance were gained through t-SNE analysis, as shown in Figures 8(d) and S7(d). The visualizations reveal distinct clustering of phenol, catechol, and *p*-nitrophenol classes, supporting the strong classification results achieved by the LR, RF, and KNN models. While the clusters are generally well separated, some overlap is evident at class boundaries, particularly where the electrochemical signals are less distinct. This partial overlap has likely contributed to the comparatively weaker performance of the SVM model, which may have struggled to define optimal decision boundaries in these ambiguous regions.

Interestingly, each cluster exhibits a radial, "flower-like" structure, which reflects systematic variation introduced by the controlled concentration gradients during the experiments. This pattern suggests that sensor responses changed consistently with analyte concentration, enhancing the discriminative power of the feature space and contributing to the high precision, recall, and F1 scores observed for LR, RF, and KNN.

In contrast, SVM's suboptimal classification performance—despite a high ROC AUC—can be attributed to limitations in kernel or parameter selection. The model's difficulty in capturing the structure of a well-separated but potentially nonlinear partition highlights the importance of appropriate

https://doi.org/10.1021/acsanm.5c03716
ACS Appl. Nano Mater. 2025, 8, 20463−20476

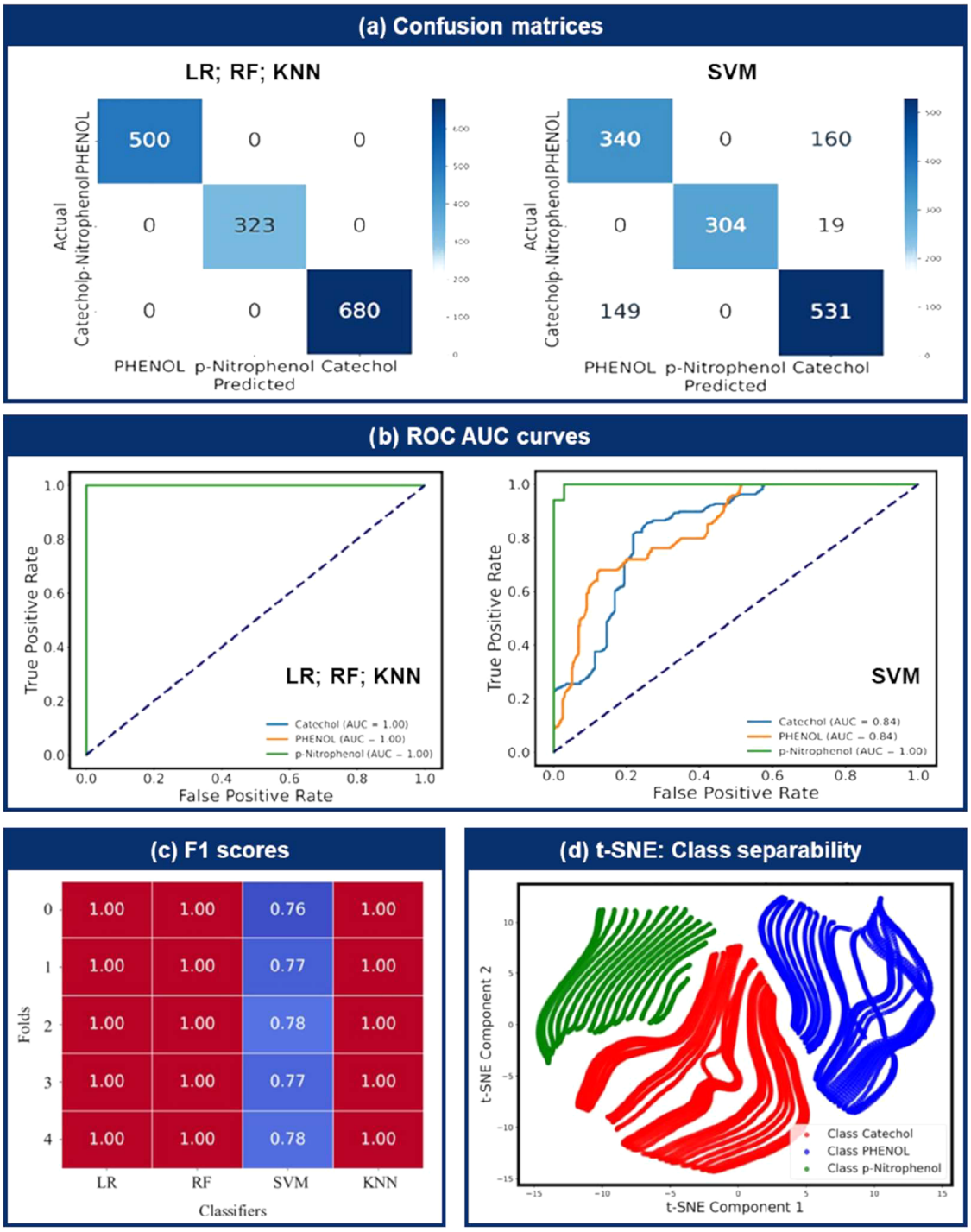

Figure 8. Machine learning analysis based on α-Ni(OH)$_2$/GCE-derived CV data: (a) confusion matrices for LR, RF, KNN (left panel), and SVM (right panel); (b) comparison of ROC AUC values across models; (c) performance assessment using 5-fold cross-validation to address potential overfitting and data consistency; (d) t-SNE visualization of the feature space showing separation of phenol, catechol, and *p*-nitrophenol. Components 1 and 2 denote the first two dimensions of the 2D embedding.

kernel tuning when applying SVMs to electrochemical sensor data.

4. CONCLUSIONS

The present work demonstrates the development of pristine nanostructured α-Ni(OH)$_2$-based electrochemical sensors in two distinct architectures—modified glassy carbon electrodes (GCE) and screen-printed carbon electrodes (SPCE)—for the sensitive and selective detection of the phenolic compounds phenol, catechol, and *p*-nitrophenol. Unlike conventional enzymatic sensors, the proposed system operates nonenzymatically, offering improved stability, simplicity, and reusability.

The nanostructured α-Ni(OH)$_2$ material, synthesized via a wet-chemical route, was deposited onto both GCE and SPCE surfaces and exhibited well-defined cyclic voltammetric responses for each analyte at characteristic potentials. Microscopy and diffraction confirmed semicrystalline nanoscale features (turbostratic layered domains and lattice fringes),

https://doi.org/10.1021/acsanm.5c03716
ACS Appl. Nano Mater. 2025, 8, 20463−20476

which increase the density of active NiOOH sites and facilitate rapid mass/electron transport. This enabled selective, room-temperature detection of multiple phenolic compounds using a single sensing platform. Among the analytes tested, phenol exhibited the highest sensitivity. The limits of detection (LODs) for the α-Ni(OH)$_2$/GCE sensor were 0.003 μM (phenol), 0.1 μM (catechol), and 1 μM (*p*-nitrophenol), while the corresponding LODs for the α-Ni(OH)$_2$/SPCE sensor were 0.3, 1, and 2 μM, respectively. Amperometric validation—including selectivity tests against common electroactive interferents—was performed for all three analytes, confirming the robustness of the α-Ni(OH)$_2$/GCE platform for quantitative detection of phenolic contaminants. While the GCE-based sensor demonstrated superior analytical performance, the SPCE configuration offers advantages for portable and field-deployable applications.

Comprehensive structural and morphological characterizations confirmed the successful synthesis of nanostructured α-Ni(OH)$_2$. Furthermore, integrating machine-learning algorithms enabled accurate classification of analyte type based on electrochemical signals from both electrode platforms. Logistic regression, random forest, and k-nearest neighbors models achieved perfect classification scores, demonstrating the strong consistency and discriminative power of the sensor outputs.

Together, these results demonstrate a versatile sensing platform that combines rational nanoscale material design, mechanistic understanding, and data-driven analysis. The nanostructured α-Ni(OH)$_2$-based system offers a reliable and scalable approach for real-time monitoring of phenolic contaminants in environmental and industrial contexts.

■ ASSOCIATED CONTENT

Supporting Information

The Supporting Information is available free of charge at https://pubs.acs.org/doi/10.1021/acsanm.5c03716.

Additional experimental details, materials, and methods (PBS preparation, real-sample spiking, electrochemical protocols, and ML workflow), plus expanded characterizations (FESEM/TEM/FTIR/Raman/XRD and post-sensing PXRD/XPS), interference tests, calibration plots, and supplementary ML figures (confusion matrices, ROC AUC, t-SNE) (PDF)

■ AUTHOR INFORMATION

Corresponding Authors

Felipe Fantuzzi − *Chemistry and Forensic Science, School of Natural Sciences, University of Kent, Canterbury CT2 7NH, U.K.;* orcid.org/0000-0002-8200-8262; Email: f.fantuzzi@kent.ac.uk

Amitava Choudhury − *Department of Computer Science and Engineering, Pandit Deendayal Energy University, Gandhinagar, Gujarat 382426, India*; Email: Amitava.choudhury@sot.pdpu.ac.in

Kalisadhan Mukherjee − *Department of Chemistry, Pandit Deendayal Energy University, Gandhinagar, Gujarat 382426, India;* orcid.org/0000-0002-5431-4246; Email: kalisadhan.mukherjee@sot.pdpu.ac.in

Authors

Suman Mondal − *Department of Chemistry, Pandit Deendayal Energy University, Gandhinagar, Gujarat 382426, India*

Aritra Roy − *Department of Chemical and Energy Engineering, London South Bank University, London SE1 0AA, U.K.;* orcid.org/0000-0003-0243-9124

Rene Pfeifer − *Centre for Cooperative Research in Biomaterials (CIC biomaGUNE), Basque Research and Technology Alliance (BRTA), Donostia-San Sebastián 20014, Spain;* orcid.org/0000-0002-0750-1321

Complete contact information is available at: https://pubs.acs.org/10.1021/acsanm.5c03716

Notes

The authors declare no competing financial interest.

■ ACKNOWLEDGMENTS

We acknowledge support from the Department of Science and Technology, Government of India (grant CRG/2022/003215). We also thank the Department of Chemistry, Pandit Deendayal Energy University, for institutional support. F.F. acknowledges the Royal Society ISPF International Collaboration Awards 2024 (Brazil and South Africa) under Grant No. [ICAO\R1\241112] for the NUBIAN project. Technical and professional assistance from Mr. Rathindranath Biswas, Mr. Shouvik Mete, Mr. Tarak Nath Das, and Mr. Ayan Roy is gratefully acknowledged.

■ REFERENCES

(1) Yang, Y.; Zhu, H.; Xu, X.; Bao, L.; Wang, Y.; Lin, H.; Zheng, C. Construction of a novel lanthanum carbonate-grafted ZSM-5 zeolite for effective highly selective phosphate removal from wastewater. *Microporous Mesoporous Mater.* **2021**, *324*, No. 111289.

(2) Karimi-Maleh, H.; Karaman, C.; Karaman, O.; Karimi, F.; Vasseghian, Y.; Fu, L.; Baghayeri, M.; Rouhi, J.; Senthil Kumar, P.; Show, P.-L.; et al. Nanochemistry approach for the fabrication of Fe and N co-decorated biomass-derived activated carbon frameworks: a promising oxygen reduction reaction electrocatalyst in neutral media. *J. Nanostructure Chem.* **2022**, *12* (3), 429−439.

(3) Madhu, R.; Karuppiah, C.; Chen, S.-M.; Veerakumar, P.; Liu, S.-B. Electrochemical detection of 4-nitrophenol based on biomass derived activated carbons. *Anal. Methods* **2014**, *6* (14), 5274−5280.

(4) Rajkumar, C.; Thirumalraj, B.; Chen, S.-M.; Veerakumar, P.; Lin, K.-C. Voltammetric determination of catechol and hydroquinone using nitrogen-doped multiwalled carbon nanotubes modified with nickel nanoparticles. *Microchim. Acta* **2018**, *185* (8), 395.

(5) Veerakumar, P.; Sangili, A.; Chen, S.-M.; Vinothkumar, V.; Kim, T. H. Octahedral Pt−Ni Alloy Nanoparticles Decorated on 3D Interconnected Porous Carbon Nanosheets for Voltammetric Determination of Dihydroxybenzene Isomers. *ACS Appl. Nano Mater.* **2023**, *6* (21), 19981−19996.

(6) Romagnoli, E.; Barboni, T.; Santoni, P.-A.; Chiaramonti, N. Quantification of volatile organic compounds in smoke from prescribed burning and comparison with occupational exposure limits. *Nat. Hazards Earth Syst. Sci.* **2014**, *14* (5), 1049−1057.

(7) Zhong, C.; He, M.; Liao, H.; Chen, B.; Wang, C.; Hu, B. Polydimethylsiloxane/covalent triazine frameworks coated stir bar sorptive extraction coupled with high performance liquid chromatography-ultraviolet detection for the determination of phenols in environmental water samples. *J. Chromatogr. A* **2016**, *1441*, 8−15.

(8) Li, X.; Xue, A.; Chen, H.; Li, S. Low-density solvent-based dispersive liquid−liquid microextraction combined with single-drop microextraction for the fast determination of chlorophenols in environmental water samples by high performance liquid chromatography-ultraviolet detection. *J. Chromatogr. A* **2013**, *1280*, 9−15.

(9) Arfin, T.; Rangari, S. N. Graphene oxide−ZnO nanocomposite modified electrode for the detection of phenol. *Anal. Methods* **2018**, *10* (3), 347−358.

(10) Zhao, L.; Lee, H. K. Determination of phenols in water using liquid phase microextraction with back extraction combined with high-performance liquid chromatography. *J. Chromatogr. A* **2001**, *931* (1−2), 95−105.
(11) Beitollahi, H.; Tajik, S.; Biparva, P. Electrochemical determination of sulfite and phenol using a carbon paste electrode modified with ionic liquids and graphene nanosheets: application to determination of sulfite and phenol in real samples. *Measurement* **2014**, *56*, 170−177.
(12) Park, S.; Kwak, D.-e.; Haque, A.-M. J.; Lee, N.-S.; Yoon, Y. H.; Yang, H. Phenolic tyrosinase substrate with a formal potential lower than that of phenol to obtain a sensitive electrochemical immunosensor. *ACS Sensors* **2022**, *7* (3), 790−796.
(13) Govindaraj, M.; Srivastava, A.; Muthukumaran, M. K.; Tsai, P.-C.; Lin, Y.-C.; Raja, B. K.; Rajendran, J.; Ponnusamy, V. K.; Selvi, J. A. Current advancements and prospects of enzymatic and non-enzymatic electrochemical glucose sensors. *Int. J. Biol. Macromol.* **2023**, *253*, No. 126680.
(14) Matos-Peralta, Y.; Gao, Z.; Mocerino, F.; Santato, C. Polyphenols on Carbon Paper Electrodes: A Fundamental Study for Sustainable Electrochemical Energy Storage. *ACS Appl. Energy Mater.* **2025**, *8* (1), 538−551.
(15) Gusmão, R.; López-Puente, V.; Pastoriza-Santos, I.; Pérez-Juste, J.; Proença, M. F.; Bento, F.; Geraldo, D.; Paiva, M. C.; González-Romero, E. Enhanced electrochemical sensing of polyphenols by an oxygen-mediated surface. *RSC Adv.* **2015**, *5* (7), 5024−5031.
(16) Pfeifer, R.; Martinhon, P. T.; Sousa, C.; Moreira, J. C.; do Nascimento, M. A. C.; Barek, J. Differential pulse voltammetric determination of 4-nitrophenol using a glassy carbon electrode: comparative study between cathodic and anodic quantification. *Int. J. Electrochem. Sci.* **2015**, *10* (9), 7261−7274.
(17) Vinoth, S.; Devi, K. S.; Pandikumar, A. A comprehensive review on graphitic carbon nitride based electrochemical and biosensors for environmental and healthcare applications. *TrAC, Trends Anal. Chem.* **2021**, *140*, No. 116274.
(18) Maikap, A.; Mukherjee, K.; Mondal, B.; Mandal, N. Zinc oxide thin film based nonenzymatic electrochemical sensor for the detection of trace level catechol. *RSC Adv.* **2016**, *6* (69), 64611−64616.
(19) Rajkumar, C.; Veerakumar, P.; Chen, S.-M.; Thirumalraj, B.; Lin, K.-C. Ultrathin sulfur-doped graphitic carbon nitride nanosheets as metal-free catalyst for electrochemical sensing and catalytic removal of 4-nitrophenol. *ACS Sustainable Chem. Eng.* **2018**, *6* (12), 16021−16031.
(20) M Visagamani, A.; Harb, M.; Kaviyarasu, K.; Muthukrishnaraj, A.; Ayyar, M.; A Alzahrani, K.; Althomali, R. H.; Althobaiti, S. A. Electrochemical detection of 4-nitrophenol using a Novel $SrTiO_3$/Ag/rGO composite. *ACS Omega* **2023**, *8* (45), 42479−42491.
(21) Jiao, L.; Xu, W.; Wu, Y.; Wang, H.; Hu, L.; Gu, W.; Zhu, C. On the road from single-atom materials to highly sensitive electrochemical sensing and biosensing. *Anal. Chem.* **2023**, *95* (1), 433−443.
(22) Lakshmi, D.; Bossi, A.; Whitcombe, M. J.; Chianella, I.; Fowler, S. A.; Subrahmanyam, S.; Piletska, E. V.; Piletsky, S. A. Electrochemical sensor for catechol and dopamine based on a catalytic molecularly imprinted polymer-conducting polymer hybrid recognition element. *Anal. Chem.* **2009**, *81* (9), 3576−3584.
(23) Zhou, Z.; Mukherjee, S.; Hou, S.; Li, W.; Elsner, M.; Fischer, R. A. Porphyrinic MOF film for multifaceted electrochemical sensing. *Angew. Chem., Int. Ed.* **2021**, *60* (37), 20551−20557.
(24) Pati, R. K.; Lee, I. C.; Gaskell, K. J.; Ehrman, S. H. Precipitation of nanocrystalline CeO_2 using triethanolamine. *Langmuir* **2009**, *25* (1), 67−70.
(25) de Hond, A. A. H.; Kant, I. M.; Honkoop, P. J.; Smith, A. D.; Steyerberg, E. W.; Sont, J. K. Machine learning did not beat logistic regression in time series prediction for severe asthma exacerbations. *Sci. Rep.* **2022**, *12* (1), No. 20363.
(26) Sipper, M.; Moore, J. H. Conservation machine learning: a case study of random forests. *Sci. Rep.* **2021**, *11* (1), No. 3629.
(27) Nagasawa, S.; Al-Naamani, E.; Saeki, A. Computer-aided screening of conjugated polymers for organic solar cell: classification by random forest. *J. Phys. Chem. Lett.* **2018**, *9* (10), 2639−2646.
(28) Pardakhti, M.; Moharreri, E.; Wanik, D.; Suib, S. L.; Srivastava, R. Machine learning using combined structural and chemical descriptors for prediction of methane adsorption performance of metal organic frameworks (MOFs). *ACS Comb. Sci.* **2017**, *19* (10), 640−645.
(29) Gao, H.; Struble, T. J.; Coley, C. W.; Wang, Y.; Green, W. H.; Jensen, K. F. Using machine learning to predict suitable conditions for organic reactions. *ACS Cent. Sci.* **2018**, *4* (11), 1465−1476.
(30) Byvatov, E.; Fechner, U.; Sadowski, J.; Schneider, G. Comparison of support vector machine and artificial neural network systems for drug/nondrug classification. *J. Chem. Inf. Comput. Sci.* **2003**, *43* (6), 1882−1889.
(31) Liu, Y. Active learning with support vector machine applied to gene expression data for cancer classification. *J. Chem. Inf. Comput. Sci.* **2004**, *44* (6), 1936−1941.
(32) Korotcov, A.; Tkachenko, V.; Russo, D. P.; Ekins, S. Comparison of deep learning with multiple machine learning methods and metrics using diverse drug discovery data sets. *Mol. Pharmaceutics* **2017**, *14* (12), 4462−4475.
(33) von Lilienfeld, O. A.; Burke, K. Retrospective on a decade of machine learning for chemical discovery. *Nat. Commun.* **2020**, *11* (1), No. 4895.
(34) Meuwly, M. Machine learning for chemical reactions. *Chem. Rev.* **2021**, *121* (16), 10218−10239.
(35) Jeevanandam, P.; Koltypin, Y.; Gedanken, A. Synthesis of nanosized α-nickel hydroxide by a sonochemical method. *Nano Lett.* **2001**, *1* (5), 263−266.
(36) Gu, F.; Cheng, X.; Wang, S.; Wang, X.; Lee, P. S. Oxidative Intercalation for Monometallic Ni^{2+}-Ni^{3+} Layered Double Hydroxide and Enhanced Capacitance in Exfoliated Nanosheets. *Small* **2015**, *11* (17), 2044−2050.
(37) Portemer, F.; Delahaye-Vidal, A.; Figlarz, M. Characterization of active material deposited at the nickel hydroxide electrode by electrochemical impregnation. *J. Electrochem. Soc.* **1992**, *139* (3), 671.
(38) Yu, X.; Zhao, J.; Zheng, L.-R.; Tong, Y.; Zhang, M.; Xu, G.; Li, C.; Ma, J.; Shi, G. Hydrogen evolution reaction in alkaline media: alpha-or beta-nickel hydroxide on the surface of platinum? *ACS Energy Lett.* **2018**, *3* (1), 237−244.
(39) Tientong, J.; Garcia, S.; Thurber, C. R.; Golden, T. D. Synthesis of nickel and nickel hydroxide nanopowders by simplified chemical reduction. *J. Nanotechnol.* **2014**, *2014* (1), No. 193162.
(40) Hall, D. S.; Lockwood, D. J.; Poirier, S.; Bock, C.; MacDougall, B. R. Raman and infrared spectroscopy of α and β phases of thin nickel hydroxide films electrochemically formed on nickel. *J. Phys. Chem. A* **2012**, *116* (25), 6771−6784.
(41) Herzberg, G. *Infrared and Raman Spectra of Polyatomic Molecules*; van Nostrand, 1945; Vol. 2.
(42) Rajamathi, M.; Kamath, P. V. On the relationship between α-nickel hydroxide and the basic salts of nickel. *J. Power Sources* **1998**, *70* (1), 118−121.
(43) Hall, D. S.; Lockwood, D. J.; Bock, C.; MacDougall, B. R. Nickel hydroxides and related materials: a review of their structures, synthesis and properties. *Proc. R. Soc. A* **2015**, *471* (2174), No. 20140792.
(44) Greczynski, G.; Hultman, L. X-ray photoelectron spectroscopy: towards reliable binding energy referencing. *Prog. Mater. Sci.* **2020**, *107*, No. 100591.
(45) Gallenberger, J.; Fernández, H. M.; Alkemper, A.; Li, M.; Tian, C.; Kaiser, B.; Hofmann, J. P. Stability and decomposition pathways of the NiOOH OER active phase of NiO x electrocatalysts at open circuit potential traced by ex situ and in situ spectroscopies. *Catal. Sci. Technol.* **2023**, *13* (16), 4693−4700.
(46) Mahala, C.; Devi Sharma, M.; Basu, M. Fe-doped nickel hydroxide/nickel oxyhydroxide function as an efficient catalyst for the oxygen evolution reaction. *ChemElectroChem* **2019**, *6* (13), 3488−3498.

https://doi.org/10.1021/acsanm.5c03716
ACS Appl. Nano Mater. 2025, 8, 20463−20476

(47) Liu, L.; Chen, X.; Qiu, J.; Hao, C. New insights into the nitroaromatics-detection mechanism of the luminescent metal−organic framework sensor. *Dalton Trans.* **2015**, *44* (6), 2897−2906.
(48) Luo, M.; Wan, D.; Chang, F. Two-dimensional Ni/Co bimetal pyrophosphate nanosheets for sensitive electrochemical detection of phenol. *Int. J. Electrochem. Sci.* **2024**, *19* (1), No. 100453.
(49) Khan, M. M.; Shaikh, H.; Al Souwaileh, A.; Khan, M. Y.; Batool, M.; Memon, S. Q.; Solangi, A. R. A highly selective nickel-aluminum layered double hydroxide nanostructures based electrochemical sensor for detection of pentachlorophenol. *Arab. J. Chem.* **2024**, *17* (3), No. 105604.
(50) Alam, M.; Srivastava, A.; Al-Otaibi, W.; Wahab, R.; Khan, S. A.; Ameen, S. Nickel-doped barium oxide nanoclusters as efficient electrode for the detection of 4-nitrophenol. *Mater. Chem. Phys.* **2024**, *328*, No. 130037.
(51) Saleem, Q.; Shahid, S.; Javed, M.; Iqbal, S.; Rahim, A.; Mansoor, S.; Bahadur, A.; Awwad, N. S.; Ibrahium, H. A.; Almufarij, R. S.; Elkaeed, E. B. Synchronized electrochemical detection of hydroquinone and catechol in real water samples using a Co@SnO_2−polyaniline composite. *RSC Adv.* **2023**, *13* (15), 10017−10028.
(52) Zhou, Y.; Zhao, J.; Li, S.; Guo, M.; Fan, Z. An electrochemical sensor for the detection of p-nitrophenol based on a cyclodextrin-decorated gold nanoparticle−mesoporous carbon hybrid. *Analyst* **2019**, *144* (14), 4400−4406.
(53) Rao, H.; Liu, Y.; Zhong, J.; Zhang, Z.; Zhao, X.; Liu, X.; Jiang, Y.; Zou, P.; Wang, X.; Wang, Y. Gold nanoparticle/chitosan@N,S co-doped multiwalled carbon nanotubes sensor: fabrication, characterization, and electrochemical detection of catechol and nitrite. *ACS Sustainable Chem. Eng.* **2017**, *5* (11), 10926−10939.
(54) Saleem, Q.; Shahid, S.; Rahim, A.; Bajaber, M. A.; Mansoor, S.; Javed, M.; Iqbal, S.; Bahadur, A.; Aljazzar, S. O.; Pashameah, R. A.; et al. A highly explicit electrochemical biosensor for catechol detection in real samples based on copper-polypyrrole. *RSC Adv.* **2023**, *13* (20), 13443−13455.
(55) Rehman, S. U.; Musuvadhi Babulal, S.; Wu, H.-F. Oxygen-Deficient Mn_2O_3 Nanosheets for Dual Colorimetric and Electrochemical Detection of Epinephrine. *ACS Appl. Nano Mater.* **2024**, *7* (21), 25004−25013.
(56) Wu, H.; Chen, Z.; Guo, L.; Wang, Y.; Du, S.; Wu, Y.; Ren, Z. Direct coupling of phthalocyanine cobalt (II) and graphene via self-driven layer-by-layer assembly for efficient electrochemical detection of catechol. *J. Electrochem. Soc.* **2020**, *167* (2), No. 027533.
(57) Kaleeswarran, P.; Sakthi Priya, T.; Chen, T.-W.; Chen, S.-M.; Kokulnathan, T.; Arumugam, A. Construction of a copper bismuthate/graphene nanocomposite for electrochemical detection of catechol. *Langmuir* **2022**, *38* (33), 10162−10172.
(58) Zhang, C.; Govindaraju, S.; Giribabu, K.; Huh, Y. S.; Yun, K. AgNWs-PANI nanocomposite based electrochemical sensor for detection of 4-nitrophenol. *Sens. Actuators B Chem.* **2017**, *252*, 616−623.
(59) Dinesh, B.; Saraswathi, R. Electrochemical synthesis of nanostructured copper-curcumin complex and its electrocatalytic application towards reduction of 4-nitrophenol. *Sens. Actuators B Chem.* **2017**, *253*, 502−512.
(60) Thangavelu, D.; Chen, Y.; Annamalai, P.; Ramadoss, M.; Narayanan, V. Rationally designed Ag@polymer@2-D LDH nanoflakes for bifunctional efficient electrochemical sensing of 4-nitrophenol and water oxidation reaction. *ACS Appl. Mater. Interfaces* **2022**, *14* (5), 6518−6527.

https://doi.org/10.1021/acsanm.5c03716
ACS Appl. Nano Mater. 2025, 8, 20463−20476